

Enhanced Molecular Spin-Photon Coupling at Superconducting Nanoconstrictions

*Ignacio Gimeno,¹ Wenzel Kersten,² María C. Pallarés,³ Pablo Hermosilla,³ María José
Martínez-Pérez,^{1,4} Mark D. Jenkins,¹ Andreas Angerer,² Carlos Sánchez-Azqueta,⁵ David
Zueco,^{1,4} Johannes Majer,^{2,6,7} Anabel Lostao,^{1,3,4} and Fernando Luis^{1,*}*

¹Instituto de Ciencia de Materiales de Aragón, CSIC-Universidad de Zaragoza, Pedro Cerbuna
12, 50009 Zaragoza, Spain

²Vienna Center for Quantum Science and Technology, Atominstitut, TU Wien, 1020 Vienna,
Austria

³Laboratorio de Microscopías Avanzadas, Instituto de Nanociencia de Aragón, Universidad de
Zaragoza, 50018 Zaragoza, Spain

⁴Fundación ARAID, Av. de Ranillas 1-D, 50018 Zaragoza, Spain

⁵Departamento de Física Aplicada, Universidad de Zaragoza, 50009 Zaragoza, Spain

⁶Shanghai Branch, CAS Center for Excellence and Synergetic Innovation Center in Quantum
Information and Quantum Physics, University of Science and Technology of China, Shanghai
201315, China

⁷National Laboratory for Physical Sciences at Microscale and Department of Modern Physics,
University of Science and Technology of China, Hefei 230026, China

Corresponding Author

*fluis@unizar.es

Supplementary Information

Fabrication of Superconducting Resonators with Nanoscopic Constrictions	p. 3
Characterization of Superconducting Resonators with Nanoscopic Constrictions	p. 5
Microwave Transmission Experiments: $w = 400\text{ }\mu\text{m}$ Resonator Coupled to a Large DPPH Pellet	p. 7
Deposition of DPPH Organic Radicals by Dip-Pen Nanolithography	p. 8
Determination of the Number N of Molecular Spins within the “Active” Region of a Nanoconstriction	p. 11
Calculation of the Collective Coupling to the Resonator	p. 13

FABRICATION OF SUPERCONDUCTING RESONATORS WITH NANOSCOPIC CONSTRICTIONS

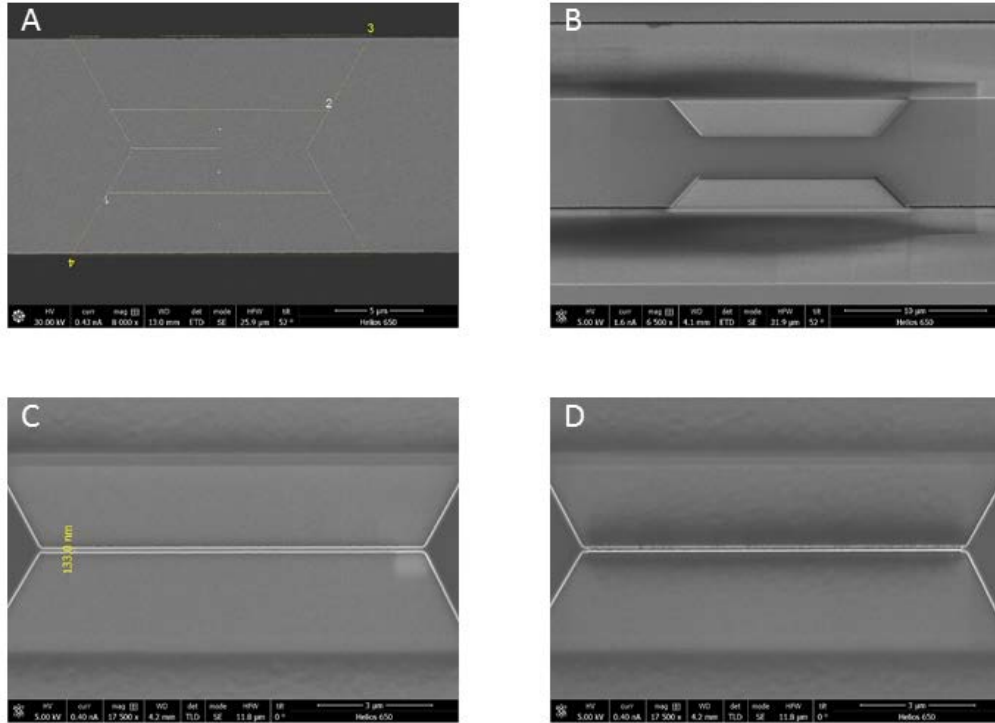


Figure S1. Fabrication steps of a superconducting nanoconstriction at the center of the transmission line of a coplanar superconducting resonator. A Ga^+ ion beam is focused onto the central line to progressively thin it down to about 42 nm.

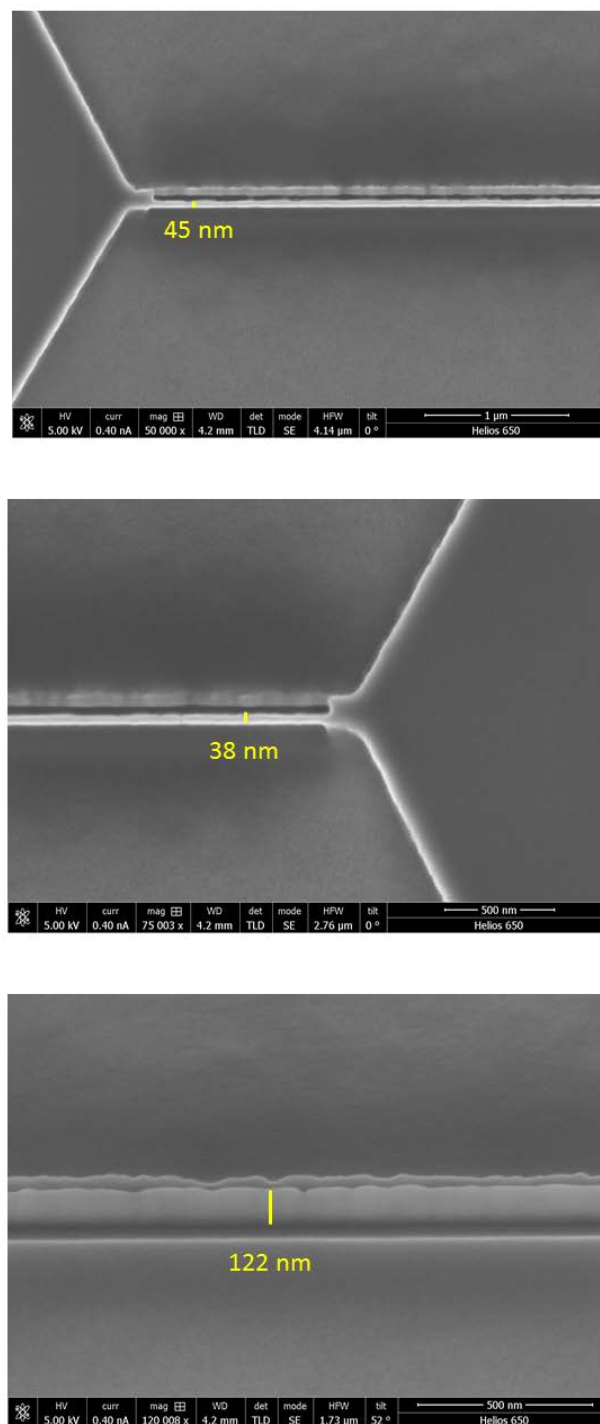


Figure S2. Close-up SEM images of the resulting 38-45 nm wide, 122 nm high constriction.

CHARACTERIZATION OF SUPERCONDUCTING RESONATORS WITH NANOSCOPIC CONSTRICTIONS

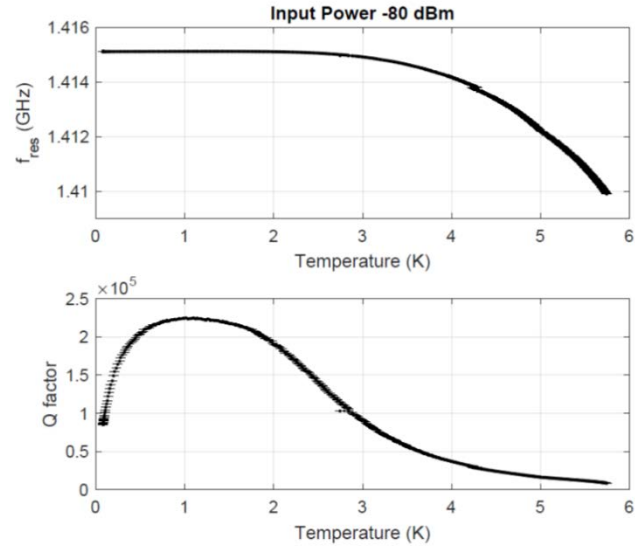


Figure S3. Variation of the resonator characteristics with temperature. Temperature dependence of the resonance frequency (top) and quality factor (bottom) of the resonator shown in figures S1 and S2.

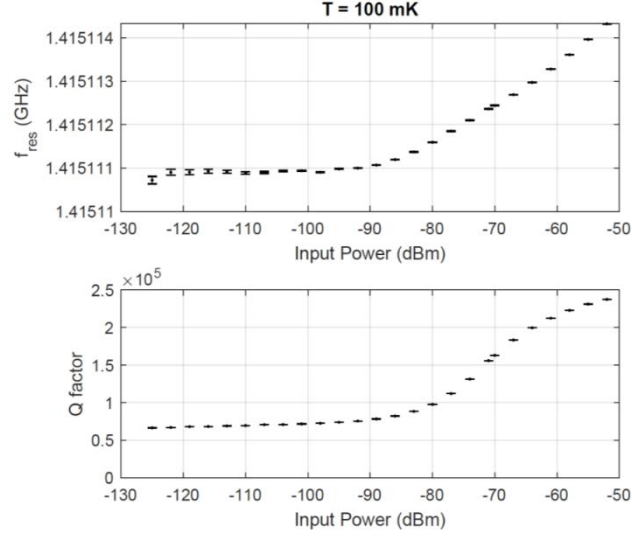


Figure S4. Input power dependence of the resonance frequency (top) and quality factor (bottom) of the resonator shown in figures S1 and S2 measured at a temperature of 100 mK.

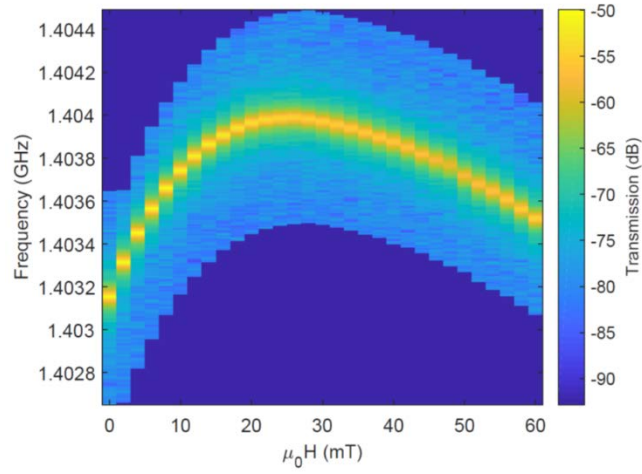


Figure S5. Magnetic field dependence of the resonant transmission of the resonator shown in Figs S1 and S2, measured at $T = 45$ mK.

MICROWAVE TRANSMISSION EXPERIMENTS: $w = 400\ \mu\text{m}$ RESONATOR COUPLED
TO A LARGE DPPH PELLET

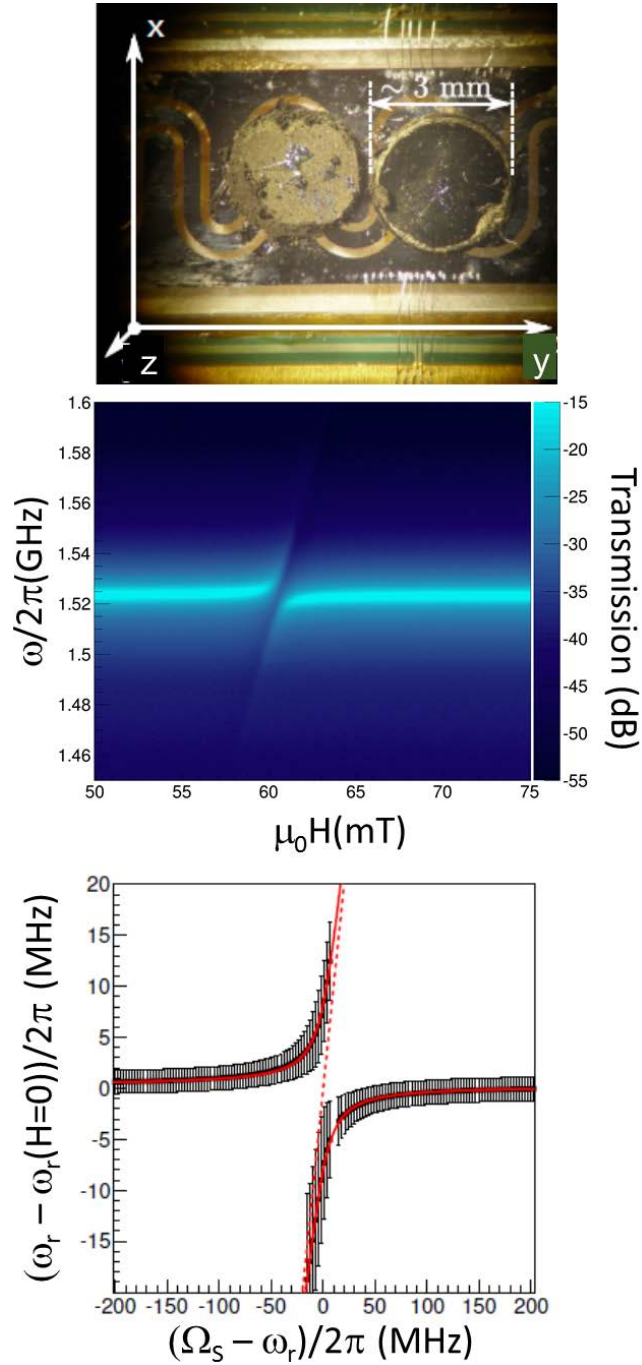


Figure S6. Strong coupling of a large DPPH ensemble to a superconducting coplanar resonator. Top: optical microscopy image of a superconducting coplanar resonator with a $400\ \mu\text{m}$

wide central transmission line hosting two pressed pellets of polycrystalline DPPH. Middle: 2D plot of the microwave transmission of this device measured at $T = 4.2$ K. Bottom: magnetic field dependence of the resonance frequency, showing the anti-crossing that is characteristic of the strong coupling regime. The solid lines are least-square fits to the equation $\omega_{\pm} = \frac{\omega_r + \Omega_S}{2} \pm \frac{\sqrt{4G_N^2 + (\Omega_S - \omega_r)^2}}{2}$, which is valid in this coupling limit and that allows determining $G_N = 8.2$ MHz.

DEPOSITION OF DPPH ORGANIC RADICALS BY DIP-PEN NANOLITHOGRAPHY

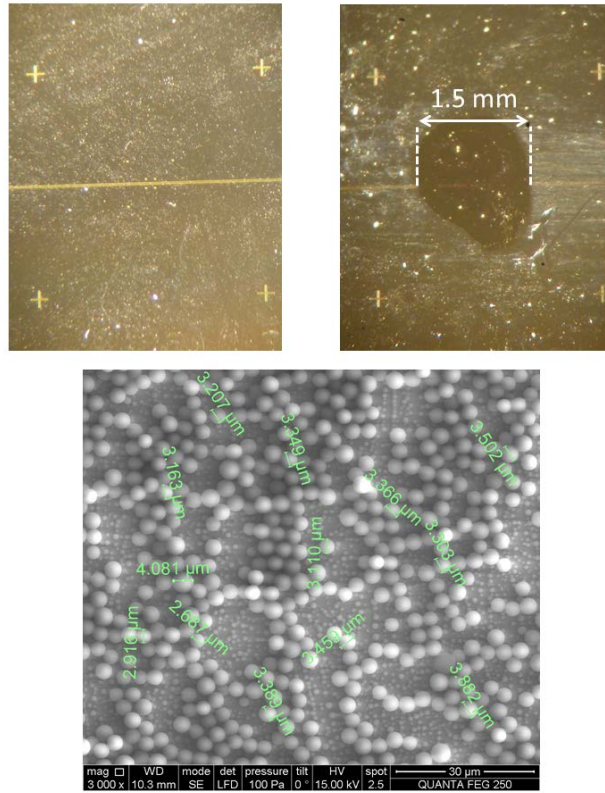


Figure S7. Deposition of macroscopic DPPH ensembles. Top: Optical microscopy images of a coplanar resonator (no constriction) before and after the deposition of a macroscopic drop of DPPH molecules. The deposition is done over the central region of the device, using a conventional

micropipette. Bottom: SEM image of the deposit after the solvent has evaporated, showing the tendency of DPPH to form aggregates.

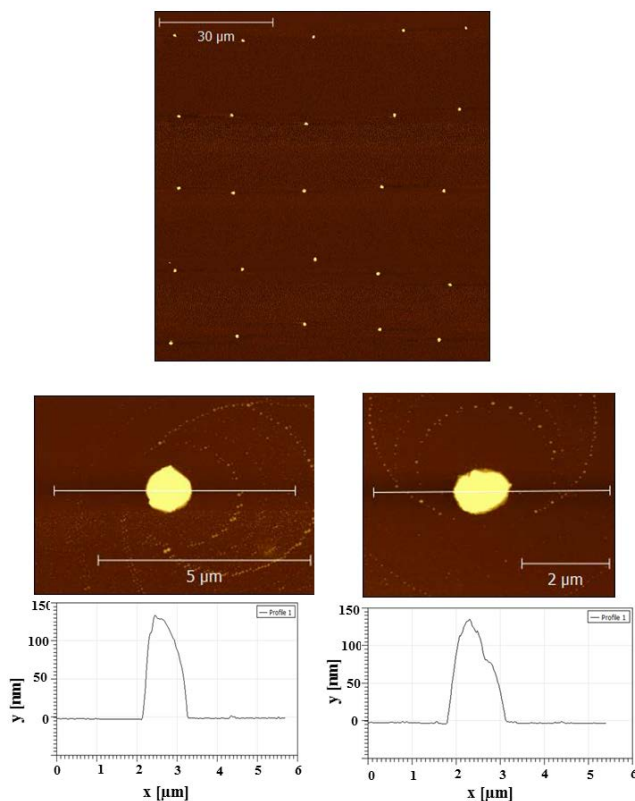


Figure S8. Control over the size and location of DPPH deposits by dip-pen nanolithography (DPN). Top: AFM image of an array of DPPH nanodroplets deposited onto a mica substrate by dip-pen nanolithography. Bottom: AFM topography images and height profiles of two of the dots measured after the solvent had evaporated.

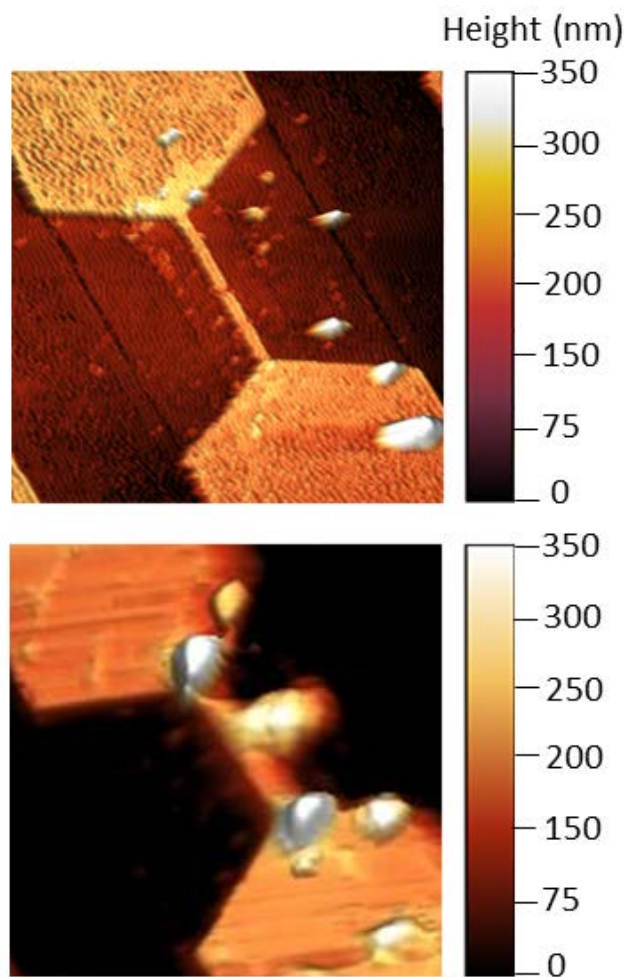


Figure S9. Deposition of DPPH nanodroplets onto superconducting nanoconstrictions. AFM 3D topography images of the same 158 nm wide constriction after two different depositions of DPPH by DPN. The one at the top gives a coupling to the resonator that is barely above the sensitivity of the experimental set-up, as no molecular nanoagglomerate has “landed” next to the constriction.

DETERMINATION OF THE NUMBER N OF MOLECULAR SPINS WITHIN THE “ACTIVE” REGION OF A NANOCONSTRICTION

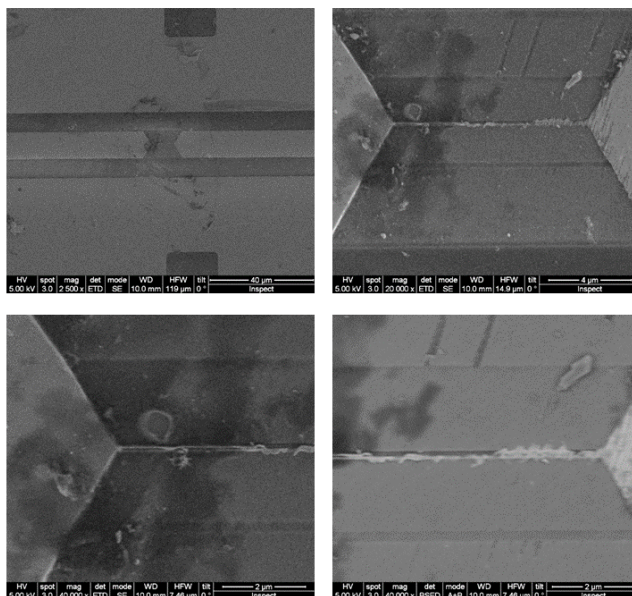


Figure S10. Characterization of DPPH deposits by Scanning Electron Microscopy (SEM). SEM images of the central region of a resonator with a 38-45 nm wide constriction. Dark areas correspond to remains of glycerol, whereas bright spots correspond to DPPH nanoagglomerates.

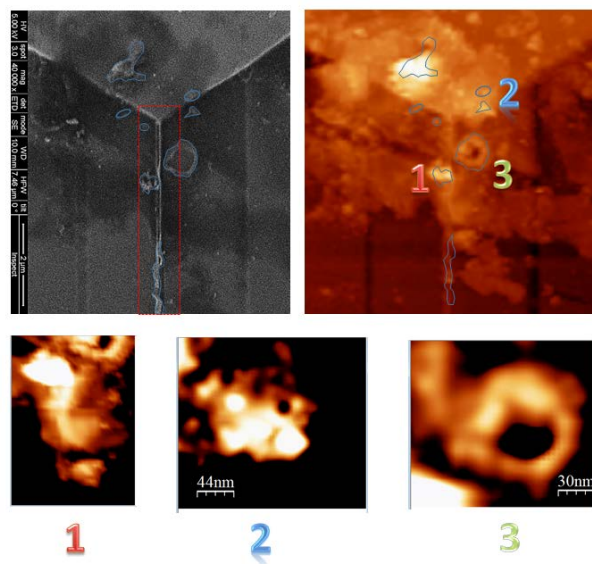


Figure S11. Determination of the number of DPPH molecules deposited. Top: SEM (left) and AFM (right) images of the same region near the nanoconstriction. Bright contrast in the SEM images signals the presence of DPPH molecules (see also Figs. S7 and S10). AFM topographic images are used to estimate the volume of all DPPH nano-agglomerates that are within 500 nm distance from the constriction (red dotted rectangle). The bottom figures show AFM images of three of these agglomerates.

CALCULATION OF THE COLLECTIVE COUPLING TO THE RESONATOR

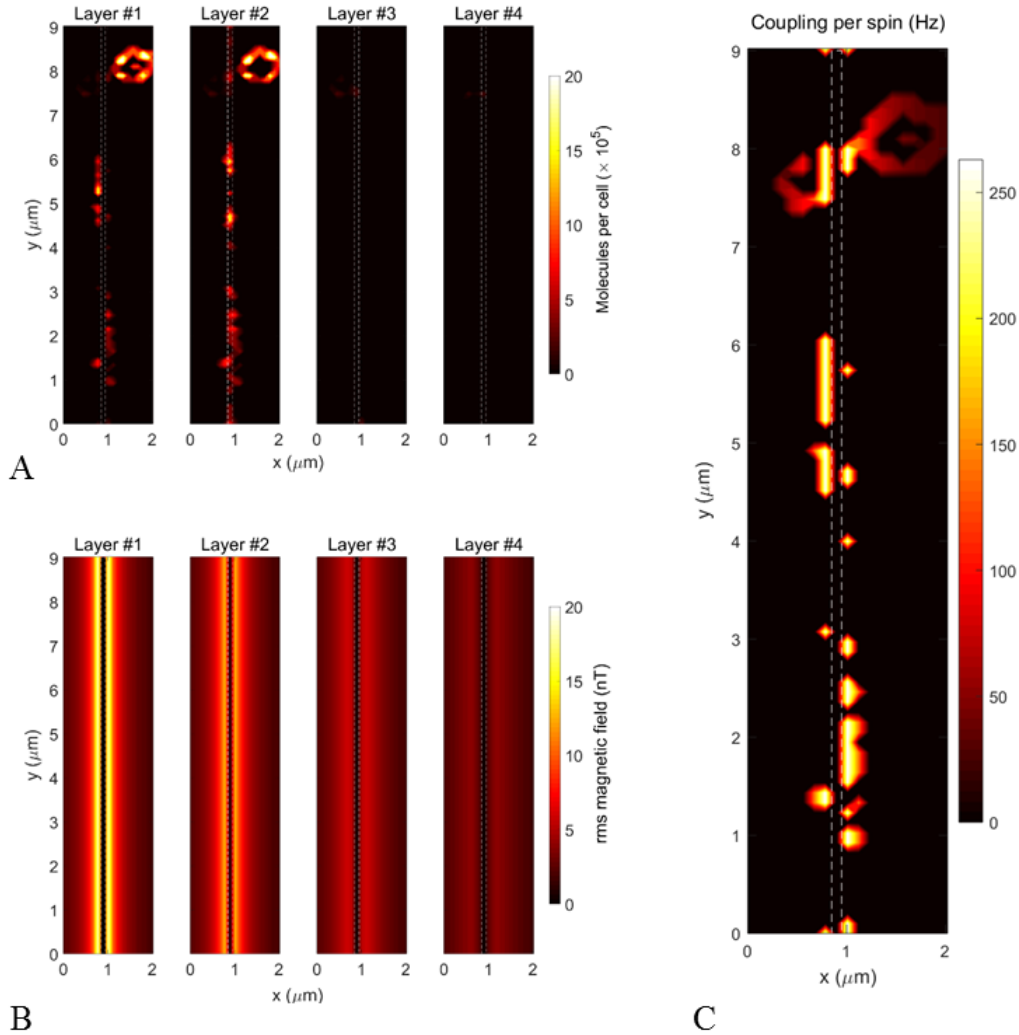


Figure S12. Finite elements calculation of the spin-photon coupling (magnetic field parallel to x). A: distribution of DPPH molecules in a three-dimensional grid centered over a 42 nm wide constriction. The cell size was $100 \times 100 \times 100 \text{ nm}^3$. The image shows the distributions in four layers located progressively farther from the chip surface (from left to right, starting from the one lying on the chip's surface). B: z component of the magnetic field $\mu_0 h$ generated by a photon at the center

of each cell. This is the component that contributes to the spin-photon coupling when the external magnetic field points along the x axis, as in the experiments described in Fig. 5 of the main text. Notice that this component vanishes at the top of the central line as indicated by the black contrast.

C: Resulting maximum coupling energy per spin. The coupling is reduced just above the nanoconstriction as a result of the vanishing $\mu_0 h_z$.

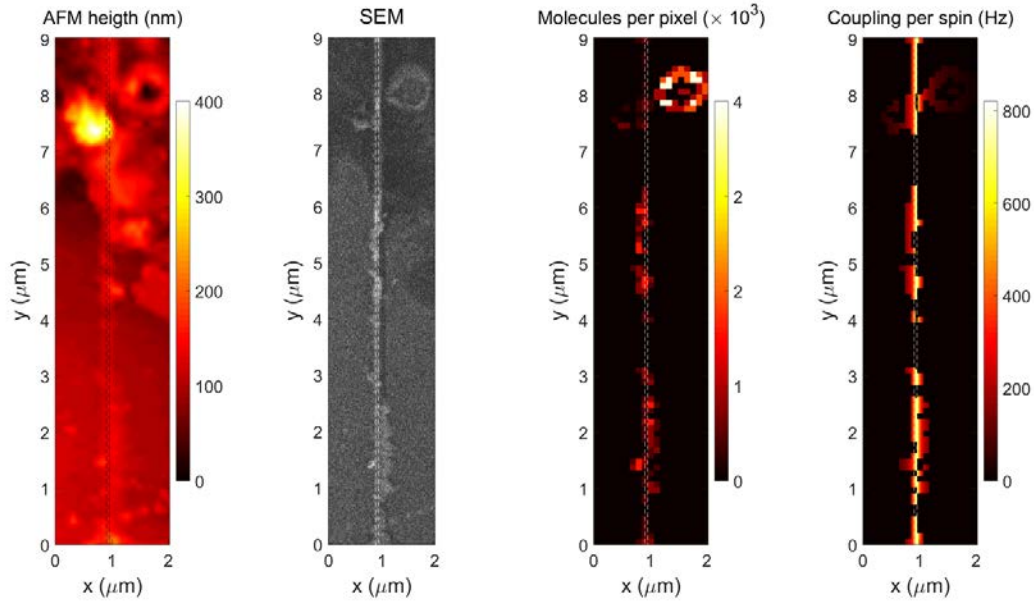


Figure S13. Spin-photon coupling for the optimal field orientation (magnetic field along y).

From left to right: AFM and SEM images of the region near a 42 nm wide nanoconstriction, color map of the number of DPPH molecules deposited on each location, and color map of the estimated single spin to photon couplings. The latter maps have been calculated with a discretization of space into $3 \times 3 \times 3 \text{ nm}^3$ cubic cells and for a magnetic field applied along the y axis, which maximizes the coupling. The number of free-radical molecules deposited in this area amounts to approximately $N = 1.6 \times 10^8$ and the collective coupling estimated from the simulations is $G_N / 2\pi = 2.6 \text{ MHz}$ at T

= 44 mK and 3.3 MHz at $T = 0$. The maximum coupling reaches values above 0.8 kHz for spins located in the close proximity of the central line.

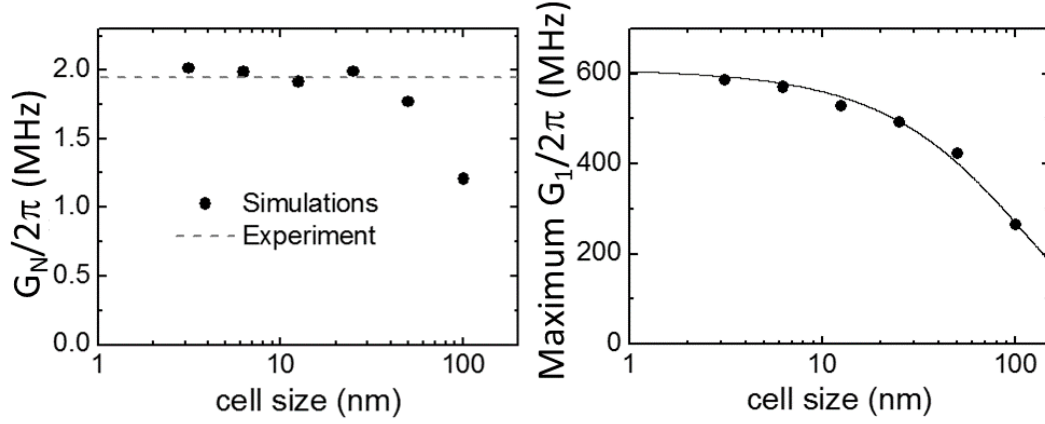


Figure S14. Determination of the optimum cell size. Collective spin-photon coupling (left) and maximum single-spin coupling energies calculated for the situation shown in Fig. S12 for varying size of the cells that form the grid. The calculations of G_N were performed for $T = 44$ mK, which corresponds to the experimental conditions of the results shown in Fig. 5 of the main text.

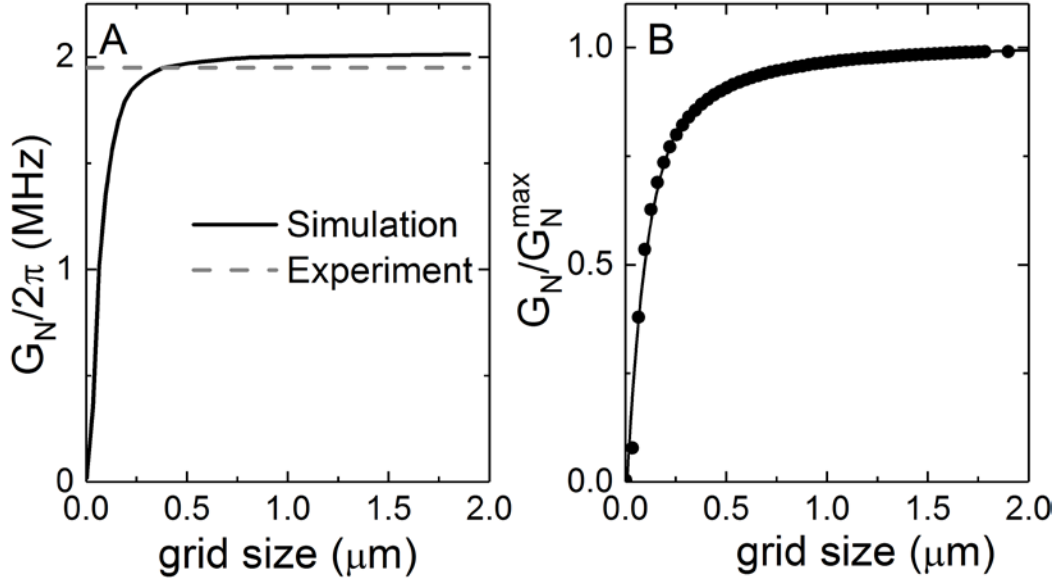


Figure S15. Determination of the optimum grid size: effective mode volume of a resonator near a superconducting nanoconstriction. A: Collective spin-photon coupling calculated for the situation shown in Fig. S12 for varying size of the grid and a fixed cell size $d = 3$ nm. The calculations were performed for $T = 44$ mK, which corresponds to the experimental conditions of the results shown in Fig. 5 of the main text. The results show that spins located beyond a distance of about 500 nm from the constriction give a close to negligible contribution. B: Results of the same calculation for the case of a homogeneously distributed molecular deposit. The width of the region that contributes most to the coupling becomes then about two times larger, showing that the coupling enhancement in A results from two combined effects: the reduce central line width and the ability to locate molecules in the optimum positions with respect to the constriction. From these results, the effective mode volume can be estimated as $\approx 1 \mu\text{m} \times 1 \mu\text{m} \times 10 \mu\text{m} = 10 \mu\text{m}^3$.

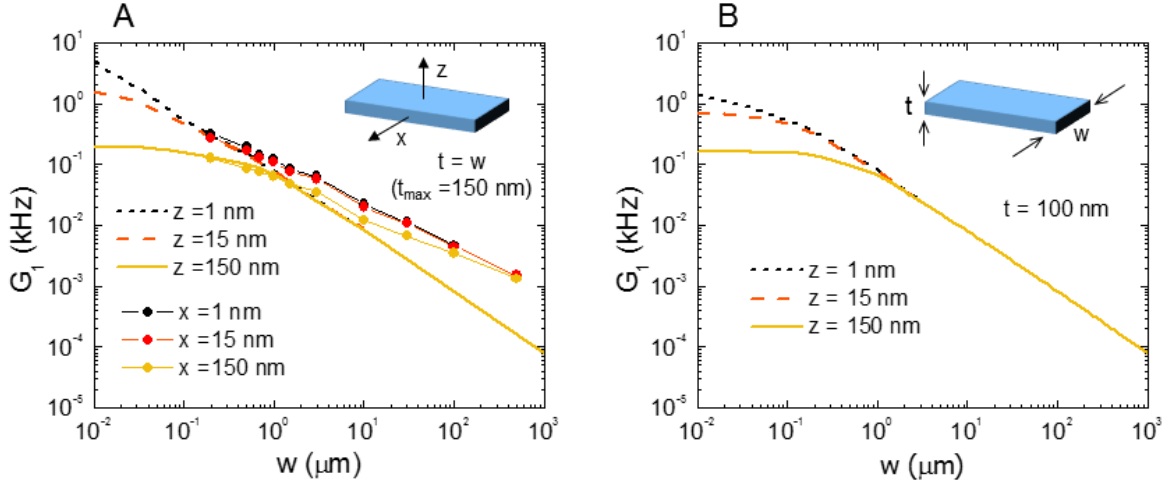


Figure S16. Single-spin coupling *versus* constriction diameter. A: Coupling to 1.4 GHz photons of individual spins located at a certain distance from the central line. As a result of the central line geometry (a slab having width w and a close to constant thickness t of about 150 nm for $w > t$ and close to w otherwise), the coupling depends on whether the spins are over the central line, and then moved along the vertical z axis from the surface, or whether they are moved within the plane (along x). For $w > 1$ μm , the probability of finding spins near the line edges, which generate stronger magnetic fields, becomes very small. For $w < 1$ μm , the difference between both situations understandably vanishes. Therefore, the coupling to spins located over the central line provides a good estimation of the “typical” single spin coupling. This choice has been used in Fig. 6 of the main text. Panel B shows G_1 calculated for a spin located over the central line but for a fixed Nb thickness $t = 100$ nm, in order to explore the effect of the constriction geometry. The results only differ from those in A for spins located very close to the surface (z close to zero) and for very narrow lines $w < 50$ nm. Even then, the differences are smaller than those associated with the spatial distribution of spins.